A regularisation technique to precisely infer limb darkening using transit measurements: can we estimate stellar surface magnetic fields?

Kuldeep Verma,[1]★ Pierre F. L. Maxted,[2]† Anjali Singh,[1]‡ H.-G. Ludwig,[3] Yashwardhan Sable [1]
[1]Department of Physics, Indian Institute of Technology (BHU), Varanasi-221005, India
[2]Astrophysics group, Keele University, Staffs, ST5 5BG, UK
[3]Landesternwarte - Zentrum für Astronomie der Universität Heidelberg, Königstuhl 12, 69117 Heidelberg, Germany

Accepted XXX. Received YYY; in original form ZZZ

ABSTRACT

The high-precision measurements of exoplanet transit light curves that are now available contain information about the planet properties, their orbital parameters, and stellar limb darkening (LD). Recent 3D magnetohydrodynamical (MHD) simulations of stellar atmospheres have shown that LD depends on the photospheric magnetic field, and hence its precise determination can be used to estimate the stellar magnetic field. Among existing LD laws, the uses of the simplest ones may lead to biased inferences, whereas the uses of complex laws typically lead to substantial degeneracy among the LD parameters. We have developed a novel approach in which we use a complex LD model but with second derivative regularisation during the fitting process. Regularisation controls the complexity of the model appropriately and reduces the degeneracy among LD parameters, thus resulting in precise inferences. The tests on simulated data suggest that our inferences are not only precise but also accurate. This technique is used to re-analyse a sample of 43 transit light curves measured by the NASA *Kepler* and TESS missions. Comparisons of our LD inferences with the corresponding literature values show good agreement, while the precisions of our measurements are better by up to 2. We find that 1D nonmagnetic model atmospheres fail to reproduce the observations while 3D MHD simulations are qualitatively consistent. The LD measurements together with the MHD simulations confirm that Kepler-17, WASP-18 and KELT-24 have relatively high magnetic fields (> 200 G). This study paves the way for estimating the stellar surface magnetic field using precise LD measurements.

Key words: method: data analysis – planets and satellites: fundamental parameters – stars: atmospheres – stars: solar-type – techniques: photometric

1 INTRODUCTION

Accurate understanding of the stellar centre-to-limb variation (CLV) of specific intensity or the so-called limb darkening (LD) is necessary to interpret a variety of astronomical observations including measurements of the exoplanet transit light curves. This becomes particularly important in the contemporary era of space-based high-precision photometry, for example from the NASA *Kepler* (Borucki et al. 2010) and Transiting Exoplanet Survey Satellite (TESS; Ricker et al. 2015), and from the upcoming ESA PLAnetary Transits and Oscillations of stars telescope (PLATO; Rauer et al. 2014). The high-quality data delivered by the James Webb Space Telescope (JWST; Gardner et al. 2006) and similar precision data expected from other upcoming facilities such as the Extremely Large Telescope (ELT; Gilmozzi & Spyromilio 2007) and Atmospheric Remote-sensing Infrared Exoplanet Large-survey (ARIEL; Tinetti et al. 2018) demand better treatment of LD. Its inadequate treatment in the analysis of the transit light curves not only limits the precision with which LD itself can be characterised, but also hinders the precision of the inferred planet and orbital properties.

Several limb darkening laws have been proposed and used in the literature. The popular ones are the linear law introduced by Milne (1921), the quadratic law (Kopal 1950), the logarithmic law (Klinglesmith & Sobieski 1970), the square-root law (Diaz-Cordoves & Gimenez 1992), the power-2 law (Hestroffer 1997), the nonlinear or Claret 4-parameter law (Claret 2000) and the exponential law proposed by Claret & Hauschildt (2003). These models of LD span a large range in complexity with the linear law, being the simplest one, has only one free parameter, whereas the non-linear law, being the most complex, has four free parameters.

The impact of uncertainty in LD models on determination of the properties of the exoplanet system has been extensively studied during the last two decades (see e.g. Sing et al. 2008; Howarth 2011; Csizmadia et al. 2013; Müller et al. 2013; Espinoza & Jordán 2016; Morello et al. 2017; Neilson et al. 2017; Patel & Espinoza 2022, just to name a few). In general, there is a consensus that the use of linear law results in biased parameter values (see e.g. Espinoza & Jordán 2016), suggesting that it is an overly simplistic model. On the other hand, the nonlinear law provides unbiased estimates (see e.g. Maxted 2023, hereafter M23). However, as can be seen in Figure 6 of M23, there are large degeneracy among the LD parameters. This could be

★ E-mail: kuldeep.phy@itbhu.ac.in (KV)
† E-mail: p.maxted@keele.ac.uk (PM)
‡ E-mail: anjalisingh.rs.phy23@itbhu.ac.in (AS)

due to inappropriate functional form of the nonlinear law or because of the fact that this model is more complex than the underlying true CLV of stars or is a combined result of both. The large degeneracy not only hampers the precision of the inferred LD parameters, but also the precision of determined planetary and orbital properties as they typically have finite correlations with the LD parameters.

The CLV of the specific intensity depends on the physical conditions near the stellar photosphere, and hence their precise measurements can provide us useful information. In fact, with the precision M23 already determined the LD parameters, he observed an on average mild but persistent systematic offset between the observed LD profiles and those predicted by various models of the stellar atmosphere. He attributed this offset to the neglect of magnetic fields in the models. Recent studies with magneto-hydrodynamical (MHD) simulations of stellar atmospheres have shown that the CLV indeed depends on the mean magnetic field in the photosphere (Norris et al. 2017; Ludwig et al. 2023; Kostogryz et al. 2024). In particular, increasing the magnetic field leads to a relative brightening of the stellar limb.

In this study, we have used the nonlinear LD model but with the second derivative regularisation while fitting the model transit light curves to the corresponding observed data. This novel approach of fitting with regularisation allows us to control the complexity of the nonlinear model appropriately, thus providing inferences of the LD parameters, planet properties, and the orbital parameters with unprecedented precision and accuracy. We test our method on 900 simulated transit light curves, and discuss its novel aspects in detail. The technique is further used to re-analyse a sample of exoplanet transit light curves measured by the *Kepler* and TESS missions to characterise them with unprecedented precision. We also analysed simulated data for an Earth-like transit expected to be observed by the PLATO satellite around a Sun-like star in the habitable zone to test whether the mission accuracy requirement on the planet-to-star radius ratio is achievable using our method.

2 TRANSIT DATA

We studied the sample of 43 stars analysed in M23. For details on the target selection and preprocessing of the transit light curves, we refer the reader to the above-mentioned paper. Briefly, the sample consists of 33 *Kepler* and 10 TESS targets. The *Kepler* targets were selected such that they had a signal-to-noise ratio greater than 500 for the transit signal, an orbital period less than 30 d, a transit impact parameter less than 0.8, and a host star effective temperature less than 7000 K. For the TESS targets, the selection was such that the host stars were brighter than the visual magnitude of 11.5 showing transits at least 0.5 per cent deep due to planets having an orbital period less than 10 d. We used the measured effective temperature $T_{\rm eff}$, surface gravity $\log g$, and metallicity [Fe/H] for all the 43 stars from M23.

3 FITTING METHOD

We use the publicly available BATMAN (version 2.4.8) package[1] (Kreidberg 2015) to calculate the model light curves for transiting exoplanets. This code has been extensively used in the literature and is well tested (see e.g. M23). BATMAN offers several options to the user for the LD model. In this study, we used it with the non-linear or the Claret 4-parameter model (Claret 2000),

$$I(\mu) = 1 - \sum_{i=1}^{4} a_i \left(1 - \mu^{i/2}\right), \tag{1}$$

where the independent variable μ is cosine of the angle θ between the surface normal vector and the line of sight, i.e. $\mu = \cos(\theta)$, and the coefficients a_1, a_2, a_3 and a_4 are constants. $I(\mu)$ is the specific intensity normalised so that $I(1) = 1$.

We used a Bayesian framework based on the Markov Chain Monte Carlo (MCMC) methods to fit the model transit light curves to the observed ones. Since there are already several text books and reviews on Bayesian statistics (see e.g. Jaynes 2003; Gelman et al. 2013) and MCMC algorithms (see e.g. Brooks et al. 2011; Sharma 2017; Hogg & Foreman-Mackey 2018), we describe them here only briefly and highlight the regularisation aspect.

In the context of parameter estimation, Bayes' theorem provides a way to update the model parameters on the basis of any new available data. In other words, it enables calculation of the posterior probability distribution (PPD) of the parameters given the new data,

$$P(\mathbf{\Theta}|\mathbf{D}) = \frac{P(\mathbf{\Theta})P(\mathbf{D}|\mathbf{\Theta})}{P(\mathbf{D})}, \tag{2}$$

where $\mathbf{D}$ represents the set of observations or the data, $\mathbf{\Theta}$ is the set of model parameters, $P(\mathbf{D}|\mathbf{\Theta}) := \mathscr{L}$ or the likelihood is the probability of observing the data given the model parameters, $P(\mathbf{\Theta})$ or the prior is the probability distribution of the model parameters before seeing the new data, and $P(\mathbf{D})$ or the evidence is the total probability of observing the data. The evidence is a normalisation constant and can be calculated by integrating the likelihood over all the model parameters.

In the current study, the observed flux as a function of time represents the data $\mathbf{D}$. Assuming the uncertainties on the flux values are independent and Gaussian distributed, we define the logarithm of the likelihood as,

$$\begin{aligned} \ln \mathscr{L} = & -\frac{1}{2}\sum_{j=1}^{N} \ln\left(2\pi f^2 \sigma_j^2\right) - \frac{1}{2}\sum_{j=1}^{N}\left(\frac{F_{{\rm obs},j} - F_{{\rm mod},j}}{f\sigma_j}\right)^2 \\ & - \frac{1}{2}\lambda^2 \sum_{j=1}^{100}\left[\frac{d^2 I(\mu)}{d\mu^2}\right]^2_{\mu=\mu_j}. \end{aligned} \tag{3}$$

The first two terms involve summation over the number of data points N in the flux time-series, and they together represent the standard logarithm of the likelihood. The quantities $F_{{\rm obs},j}$ and σ_j are the measured values of the flux and the corresponding observational uncertainty, respectively, whereas the quantity $F_{{\rm mod},j}$ is the model flux value. In equation 3, we assume that the uncertainties σ_j are well estimated, however they can be wrong by a constant factor f. This factor f is treated as a free parameter in the fitting process. The last term represents a second derivative regularisation and is proportional to the sum of squares of the second derivative of $I(\mu)$,

$$\frac{d^2 I(\mu)}{d\mu^2} = \frac{1}{4}\sum_{i=1}^{4} i(i-2)a_i \mu^{(i-4)/2}, \tag{4}$$

calculated at 100 uniformly spaced μ values between 0.01 and 1. The proportionality constant λ is called regularisation parameter. It should be noted that λ is dimensionless because $I(\mu)$ is normalised and has no dimension. The regularisation term penalises large curvatures in the LD profile to the extent determined by the value of λ (see Section 4.1). We tried the first derivative regularisation as well,

[1] https://lkreidberg.github.io/batman/docs/html/index.html

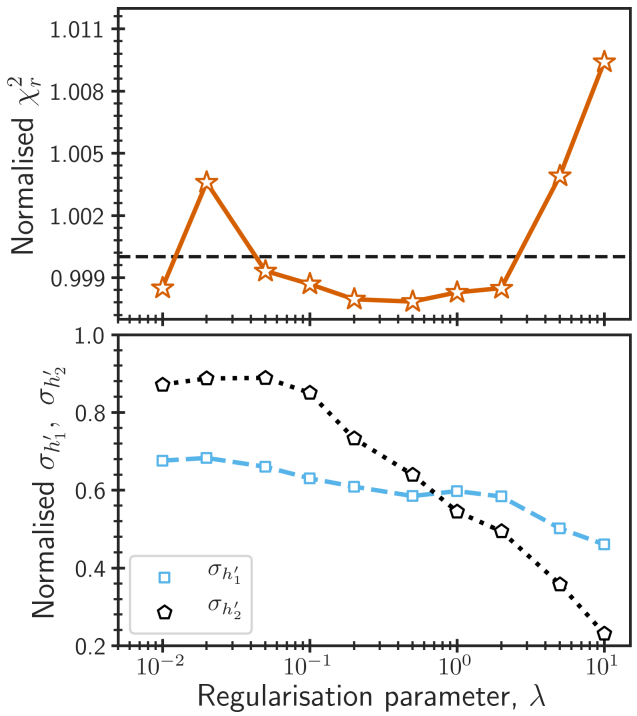

Figure 1. Reduced chi-square (top panel) and uncertainties on h'_1 and h'_2 (bottom panel) obtained by fitting the transit light curve of Kepler-5 as a function of the regularisation parameter. The χ^2_r and uncertainties are normalised such that they are 1 for the fit with $\lambda = 0$. The dashed horizontal line in the top panel marks the value of 1 for the normalised χ^2_r. As also shown in the legend, the square and pentagon symbols in the bottom panel represent normalised $\sigma_{h'_1}$ and $\sigma_{h'_2}$, respectively. The points are connected with lines to guide the eye.

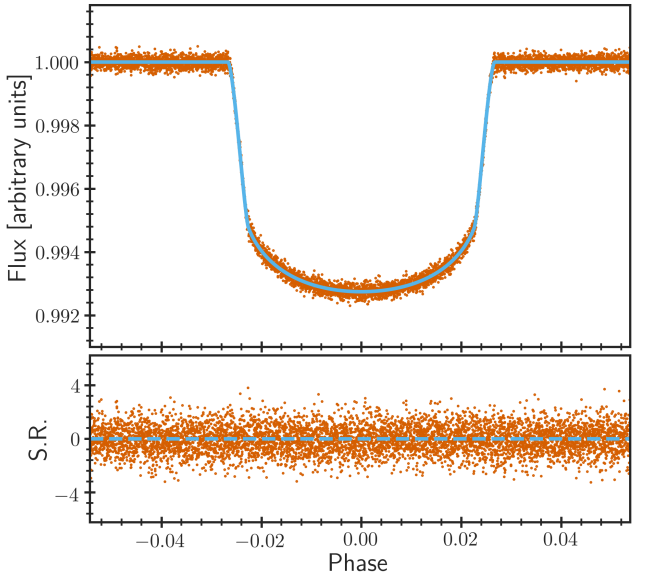

Figure 2. Phase folded light curve for Kepler-5 (top panel) and standardised residual (bottom panel). In the top panel, the dots show the observed data while the continuous curve represents the best-fitting model obtained with $\lambda = 0.2$. In the bottom panel, the standardised residual is the residual divided by the corresponding observational uncertainty. The dashed horizontal line marks the zero level.

but the preliminary results indicated substantially worse performance compared to the second derivative regularisation.

Our transit model contains a set of 10 free parameters; these are the orbital period P, the mid-transit time T_0, the planet-to-star radius ratio R_p/R_*, the ratio of the host star radius and the orbital semimajor axis R_*/a, the transit impact parameter b, the LD parameters $\{a_1, a_2, a_3, a_4\}$, and the logarithm of the error scale factor f. For all of them, we used uniform priors, viz. $P \in [0, 500]$ d, $T_0 \in [0, 2460300]$ d (the upper Julian date corresponds to a calendar date of December 21, 2023, and hence the prior covers the full time span of all the observed transit light curves analysed in this study), R_p/R_* and $R_*/a \in [0, 0.5]$, $b \in [-1, 1]$, all the LD parameters $a_i \in [-50, 50]$ and $\log f \in [-0.5, 0.5]$. Note that, in principle, T_0 can have multiple values separated by P, in practice however, the sampler finds a value closest to its initial guess (PPD remains unimodal).

Finally, we sampled the PPD defined by equation (2) using the publicly available affine invariant MCMC ensemble sampler, EMCEE: the MCMC hammer[2] (Goodman & Weare 2010; Foreman-Mackey et al. 2013). We used 100 walkers, a total of 5000 steps, and 4000 burn-in steps. The convergence of chains was confirmed by visually inspecting the trends in the parameter values and variances as a function of step number after the burn-in phase.

[2] https://emcee.readthedocs.io/en/stable/

4 RESULTS

We now test the above fitting approach using simulated data and re-analyse the observed transit light curves of stars in our sample. However, we first need to find an optimal value of λ to be used in the definition of our likelihood function.

4.1 Determining regularisation parameter

From the definition of the likelihood in equation 3, a small or close to zero value of λ would clearly mean that all LD coefficients are free to vary during the fitting process. In such a case, the four free parameters in the nonlinear law provide large flexibility in the model, and hence it reproduces the observed high-precision photometric data quite well. However, if it turns out that the true LD profiles of stars are simpler than those predicted by the nonlinear law, then its use would lead to over-fitting of data. The large degeneracies among the LD parameters as seen in M23 could potentially be a result of this. On the other hand, it may be noted again from equation 3 that a choice of an extremely large value of λ during the fitting process would lead to small values of second derivative of $I(\mu)$, as defined in equation 4, for all values of μ, i.e. $-a_1\mu^{-3/2} + 3a_3\mu^{-1/2} + 8a_4 \approx 0$. In other words, such a choice of λ would lead to a simpler LD law with only three free parameters and could lead to under-fitting of data.

To determine the optimal value of λ, we performed 11 different fits to the observed transit light curve of Kepler-5 with $\lambda = \{0, 0.01, 0.02, 0.05, 0.1, 0.2, 0.5, 1, 2, 5, 10\}$, and observed the change in the goodness of fit as defined by the reduced chi-square,

$$\chi^2_r = \frac{1}{N-10}\sum_{j=1}^{N}\left(\frac{F_{\mathrm{obs},j} - F_{\mathrm{mod},j}}{\sigma_j}\right)^2, \tag{5}$$

as function of λ in Figure 1. Note that in the above fits, except for λ, everything else, including the priors on the model parameters

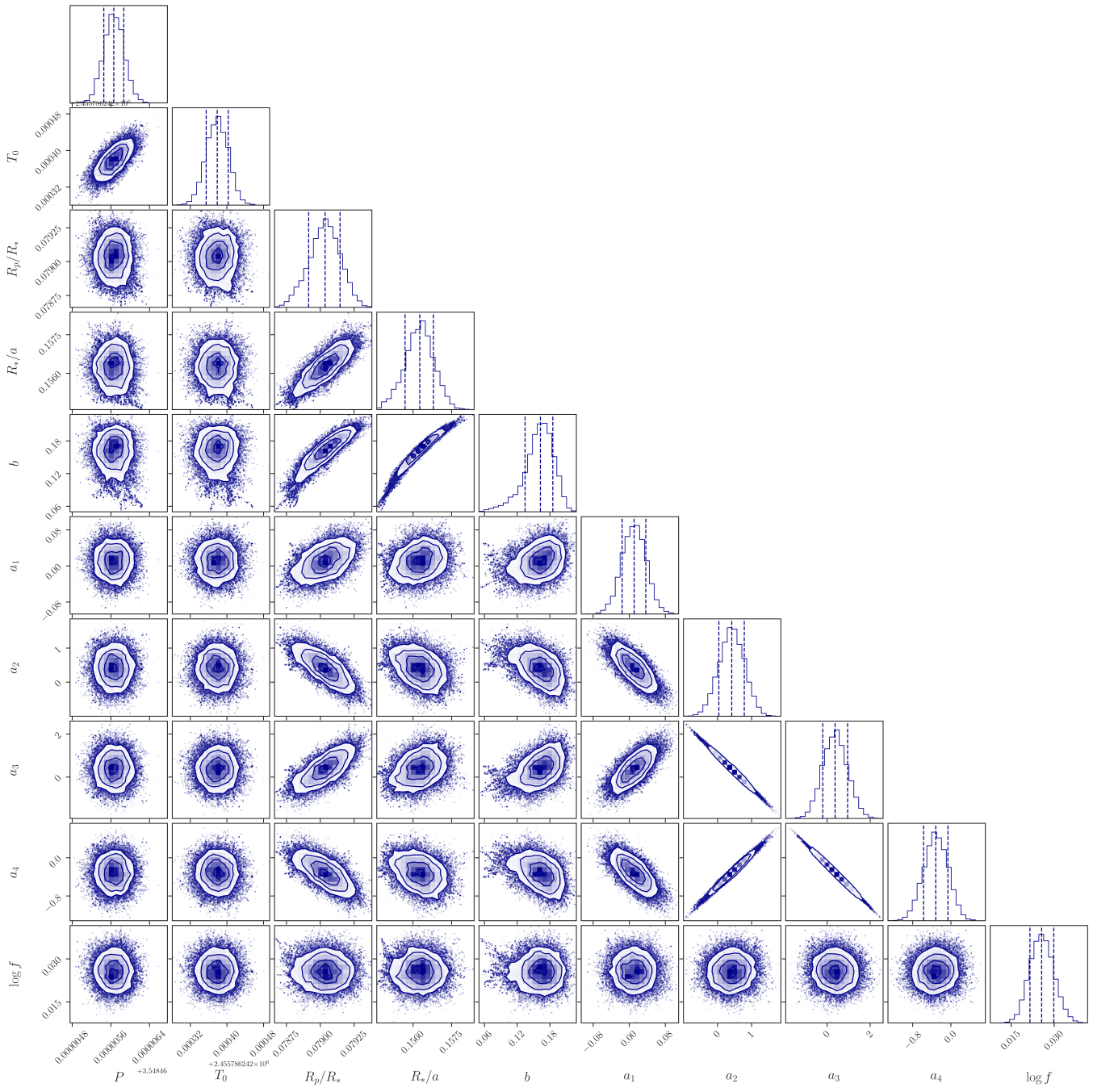

Figure 3. Corner diagram showing the PPD resulting from the fit to the transit light curve of Kepler-5 with $\lambda = 0.2$.

and the initial guesses for different walkers, remains unchanged. The values of χ^2_r are normalised such that it is 1 for the fit with $\lambda = 0$. At low values of λ, the normalised χ^2_r shows small fluctuations around the value of 1. This is likely related to small differences in the convergence of MCMC chains for the fits with different values of λ. However, the normalised χ^2_r starts to increase monotonically for $\lambda > 0.5$, indicating that the LD model is becoming increasingly simpler and inadequate to model the data. This suggests that any value with $\lambda \leq 0.5$ is a reasonable choice.

In addition to the goodness of fit, we also monitored the precision with which we could infer the LD profile using different values of λ. Since the LD parameters are strongly correlated, it is useful to introduce a new set of variables that have relatively low correlations (see e.g. Maxted 2018, 2023). We shall use the parameters h'_1 and h'_2 defined in M23 as,

$$h'_1 = I(\mu = 2/3) \tag{6}$$

and

$$h'_2 = h'_1 - I(\mu = 1/3), \tag{7}$$

to characterise the LD profile. Given the LD coefficients a_i, these new parameters can easily be calculated using the equation 1. In the

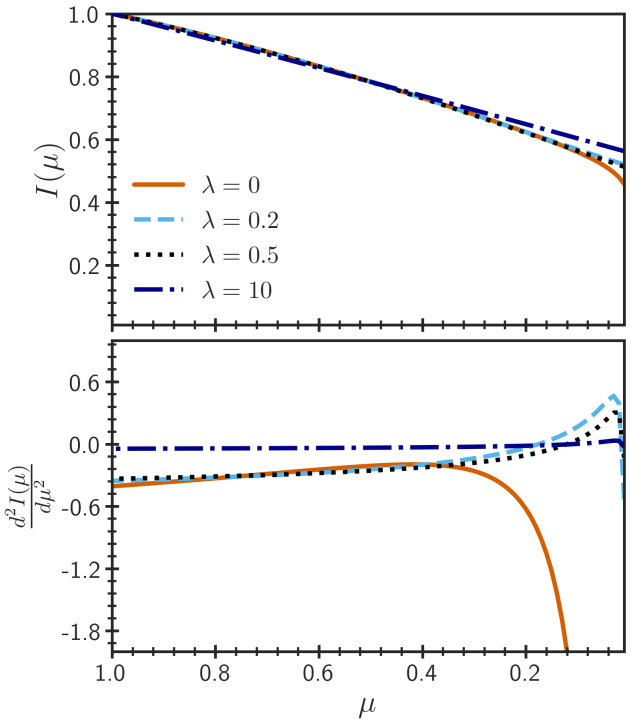

Figure 4. Limb darkening profiles (top panel) and their second derivatives (bottom panel) as obtained by fitting the transit light curve of Kepler-5 with different values of regularisation parameter. As indicated in the legend, the solid, dashed, dotted, and dash-dotted curves represent profiles with λ = 0, 0.2, 0.5, and 10, respectively. In the bottom panel, the y-axis is restricted in the range from -2 to 1 for clarity.

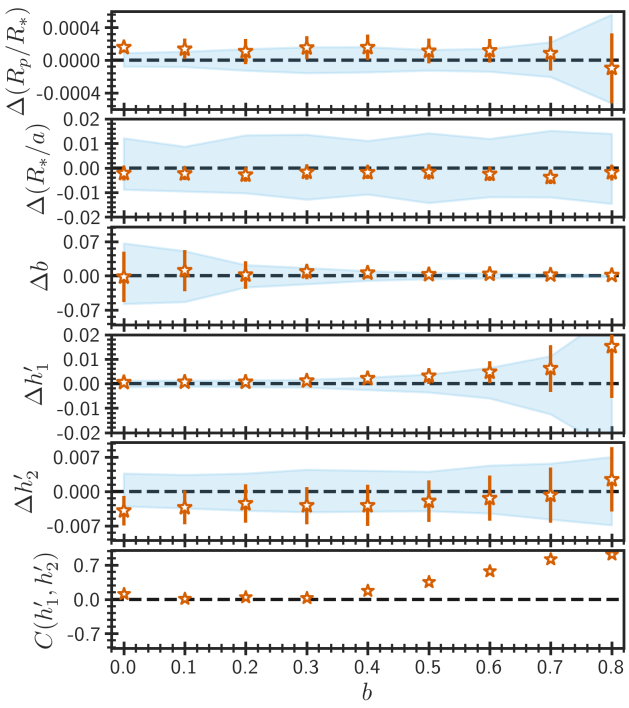

Figure 5. The orbital and limb darkening parameters recovered from the simulated light curves of a transiting hot Jupiter using our fitting method with λ = 0.2. The points at different b values with errorbar show the differences between the mean values of parameters obtained by fitting the 100 simulations and the corresponding true values. The errorbars are the standard deviations computed using the 100 realisations. The shaded regions represent the uncertainties calculated from the PPD of one simulation at a given b. In the bottom panel, the points show correlation between h_1' and h_2' computed using the PPD of one simulation at a given b. The horizontal dashed lines correspond to perfect recovery in the top five panels, while in the bottom panel it marks zero correlation between h_1' and h_2'.

bottom panel of Figure 1, we show the inferred uncertainties in h_1' and h_2' as a function of λ. Again, the uncertainties are normalised such that they are 1 for the fit with $\lambda = 0$. The uncertainties in both h_1' and h_2' decrease with increasing λ. This is expected as higher values of λ lead to tighter constraints on the LD profile.

Based on the above results, it is tempting to choose $\lambda = 0.5$ as the optimal value because it not only keeps χ_r^2 at a minimum level, but also maximises the precision of h_1' and h_2' for $\lambda \leq 0.5$. However, we wish to point out that there is a small chance that $\lambda = 0.5$ is already oversimplifying the LD model and the resulting slightly smaller χ_r^2 value compared to the case of $\lambda = 0.2$ is just due to differences in the convergence of MCMC chains. To avoid potential biases in our inferences due to the oversimplification of the LD model, we give up the precision of h_1' and h_2' slightly and take instead $\lambda = 0.2$ as the optimal or reference value and use it from now on (unless mentioned otherwise). This choice provides good fit to the data, as seen in Figure 2, and results in reasonably precise LD parameters. As we can see in the corner plot (Foreman-Mackey 2016) in Figure 3, the distributions are unimodal and the model parameters are well determined. Furthermore, the degeneracy among the LD parameters are much smaller (especially between a_1 and a_2, a_1 and a_3, and a_1 and a_4) compared to that found in M23 (see their Figure 6).

The top panel of Figure 4 presents the LD profiles of Kepler-5 obtained by fitting its transit light curve with four different values of λ. Clearly, all the profiles look similar for $\mu \gtrapprox 0.2$, indicating that this part of the profile is well constrained by the observational data. On the other hand, regularisation has significant impact on part of the profile close to the limb ($\mu \lessapprox 0.2$) where it systematically pushes the profile upward. The bottom panel shows the curvature profile. As expected, the LD profile obtained with $\lambda = 0$ has large magnitudes of the curvature (larger than 2 near the limb), while the one with $\lambda = 10$ has a curvature approaching zero. The detailed implications of choosing different values of λ compared to the reference value of 0.2 are discussed in Section A.

4.2 Test on simulated data

To test the accuracy of our inferences, we generated a set of 900 simulated transit light curves for 9 uniformly spaced b values between 0 and 0.8 using BATMAN. In the simulations, we assumed P = 3.5 d, R_p/R_* = 0.08, R_*/a = 0.15 and the solar LD profile computed by Kostogryz et al. (2022). The light curves were sampled at 2000 points uniformly distributed throughout the duration of the transit. For each value of b, we generated 100 light curves including Gaussian random noise with a standard deviation of 100 ppm per observation. This is similar to the signal-to-noise in the *Kepler* light curves of moderately bright stars like Kepler-5 with transiting hot Jupiters.

We fitted all the 900 simulated light curves with the reference value of λ = 0.2. For each value of b, we use the 100 simulations to compute the mean and standard deviation of the parameters and compare them with the corresponding true values in Figure 5. All

Table 1. Inferred parameters for Kepler-5 from M23 and this work (V24 and V24test; see the related text for details).

Work	P [d]	h'_1	h'_2	$C(h'_1, h'_2)$	R_p/R_*	R_*/a	b	f
M23	3.55	0.863 ± 0.001	0.168 ± 0.005	−0.15	0.0789 ± 0.0002	0.1563 ± 0.0006	0.15 ± 0.03	1.06
V24	3.55	$0.864^{+0.002}_{-0.002}$	$0.169^{+0.005}_{-0.005}$	−0.42	$0.0790^{+0.0003}_{-0.0004}$	$0.1564^{+0.0006}_{-0.0007}$	$0.16^{+0.03}_{-0.04}$	1.06
V24test	3.55	$0.863^{+0.001}_{-0.001}$	$0.168^{+0.004}_{-0.004}$	−0.19	$0.0789^{+0.0002}_{-0.0002}$	$0.1564^{+0.0006}_{-0.0006}$	$0.16^{+0.03}_{-0.03}$	1.06

Table 2. Inferred parameters for all the targets in our sample. Orbital period has no statistical error at the fourth decimal place.

Star	P [d]	h'_1	h'_2	$C(h'_1, h'_2)$	R_p/R_*	R_*/a	b	$log f$	χ^2_r
HAT-P-7	2.2047	$0.8586^{+0.0009}_{-0.0010}$	$0.1761^{+0.0009}_{-0.0008}$	−0.03	$0.07747^{+0.00003}_{-0.00003}$	$0.2406^{+0.0002}_{-0.0002}$	$0.492^{+0.001}_{-0.001}$	$0.115^{+0.003}_{-0.003}$	1.70
Kepler-4	3.2137	$0.8494^{+0.0096}_{-0.0086}$	$0.2227^{+0.0105}_{-0.0096}$	0.51	$0.02468^{+0.00025}_{-0.00023}$	$0.1667^{+0.0078}_{-0.0066}$	$0.344^{+0.102}_{-0.141}$	$0.038^{+0.005}_{-0.005}$	1.20
Kepler-5	3.5485	$0.8637^{+0.0011}_{-0.0011}$	$0.1681^{+0.0036}_{-0.0035}$	0.02	$0.07903^{+0.00011}_{-0.00012}$	$0.1563^{+0.0005}_{-0.0006}$	$0.163^{+0.023}_{-0.028}$	$0.026^{+0.004}_{-0.004}$	1.13
Kepler-6	3.2347	$0.8229^{+0.0010}_{-0.0009}$	$0.2092^{+0.0041}_{-0.0038}$	−0.20	$0.09174^{+0.00016}_{-0.00017}$	$0.1339^{+0.0004}_{-0.0005}$	$0.167^{+0.021}_{-0.027}$	$0.018^{+0.005}_{-0.005}$	1.09
Kepler-7	4.8855	$0.8548^{+0.0045}_{-0.0046}$	$0.1894^{+0.0038}_{-0.0037}$	0.43	$0.08236^{+0.00012}_{-0.00012}$	$0.1505^{+0.0005}_{-0.0005}$	$0.559^{+0.005}_{-0.005}$	$0.033^{+0.005}_{-0.005}$	1.17
Kepler-8	3.5225	$0.8642^{+0.0151}_{-0.0148}$	$0.1796^{+0.0069}_{-0.0068}$	0.85	$0.09458^{+0.00028}_{-0.00028}$	$0.1466^{+0.0004}_{-0.0004}$	$0.722^{+0.002}_{-0.002}$	$0.022^{+0.005}_{-0.004}$	1.11
Kepler-12	4.4379	$0.8445^{+0.0008}_{-0.0008}$	$0.1864^{+0.0042}_{-0.0038}$	−0.16	$0.11779^{+0.00015}_{-0.00016}$	$0.1249^{+0.0002}_{-0.0002}$	$0.177^{+0.013}_{-0.014}$	$0.061^{+0.004}_{-0.004}$	1.33
Kepler-14	6.7901	$0.8534^{+0.0071}_{-0.0071}$	$0.1707^{+0.0038}_{-0.0035}$	0.70	$0.04552^{+0.00009}_{-0.00009}$	$0.1355^{+0.0009}_{-0.0009}$	$0.597^{+0.008}_{-0.008}$	$0.045^{+0.003}_{-0.003}$	1.23
Kepler-15	4.9428	$0.8314^{+0.0132}_{-0.0133}$	$0.2148^{+0.0098}_{-0.0095}$	0.83	$0.10273^{+0.00037}_{-0.00038}$	$0.1016^{+0.0004}_{-0.0004}$	$0.683^{+0.004}_{-0.004}$	$0.043^{+0.007}_{-0.007}$	1.22
Kepler-17	1.4857	$0.8406^{+0.0012}_{-0.0012}$	$0.1757^{+0.0047}_{-0.0046}$	−0.02	$0.13268^{+0.00020}_{-0.00020}$	$0.1765^{+0.0004}_{-0.0003}$	$0.168^{+0.015}_{-0.016}$	$0.135^{+0.006}_{-0.006}$	1.87
Kepler-41	1.8555	$0.8344^{+0.0152}_{-0.0155}$	$0.2077^{+0.0109}_{-0.0104}$	0.83	$0.10056^{+0.00041}_{-0.00042}$	$0.1961^{+0.0008}_{-0.0009}$	$0.683^{+0.005}_{-0.005}$	$0.020^{+0.009}_{-0.009}$	1.10
Kepler-43	3.0241	$0.8588^{+0.0094}_{-0.0092}$	$0.2026^{+0.0057}_{-0.0058}$	0.70	$0.08557^{+0.00018}_{-0.00018}$	$0.1445^{+0.0005}_{-0.0005}$	$0.658^{+0.004}_{-0.004}$	$0.019^{+0.005}_{-0.005}$	1.09
Kepler-44	3.2467	$0.8250^{+0.0218}_{-0.0213}$	$0.2014^{+0.0192}_{-0.0177}$	0.77	$0.08073^{+0.00070}_{-0.00064}$	$0.1436^{+0.0024}_{-0.0023}$	$0.642^{+0.018}_{-0.019}$	$0.037^{+0.008}_{-0.008}$	1.19
Kepler-45	2.4552	$0.8169^{+0.0080}_{-0.0083}$	$0.2313^{+0.0169}_{-0.0170}$	0.70	$0.18176^{+0.00080}_{-0.00082}$	$0.0931^{+0.0003}_{-0.0003}$	$0.561^{+0.006}_{-0.006}$	$0.035^{+0.006}_{-0.006}$	1.18
Kepler-74	7.3407	$0.8289^{+0.0292}_{-0.0288}$	$0.1787^{+0.0187}_{-0.0168}$	0.81	$0.09120^{+0.00071}_{-0.00074}$	$0.0655^{+0.0007}_{-0.0007}$	$0.701^{+0.010}_{-0.011}$	$0.099^{+0.008}_{-0.008}$	1.59
Kepler-77	3.5788	$0.8200^{+0.0030}_{-0.0030}$	$0.2107^{+0.0069}_{-0.0063}$	0.22	$0.09811^{+0.00027}_{-0.00028}$	$0.1035^{+0.0006}_{-0.0006}$	$0.366^{+0.015}_{-0.016}$	$0.038^{+0.007}_{-0.007}$	1.19
Kepler-412	1.7209	$0.8147^{+0.0356}_{-0.0350}$	$0.1975^{+0.0120}_{-0.0117}$	0.87	$0.10372^{+0.00090}_{-0.00084}$	$0.2052^{+0.0010}_{-0.0010}$	$0.795^{+0.003}_{-0.003}$	$0.018^{+0.010}_{-0.010}$	1.09
Kepler-422	7.8914	$0.8361^{+0.0034}_{-0.0033}$	$0.1969^{+0.0046}_{-0.0042}$	0.28	$0.09583^{+0.00015}_{-0.00017}$	$0.0736^{+0.0002}_{-0.0002}$	$0.492^{+0.006}_{-0.006}$	$0.046^{+0.004}_{-0.004}$	1.24
Kepler-423	2.6843	$0.8301^{+0.0018}_{-0.0018}$	$0.2063^{+0.0060}_{-0.0056}$	−0.01	$0.12395^{+0.00023}_{-0.00026}$	$0.1231^{+0.0003}_{-0.0003}$	$0.331^{+0.009}_{-0.010}$	$0.034^{+0.007}_{-0.007}$	1.17
Kepler-425	3.7970	$0.8020^{+0.0112}_{-0.0110}$	$0.2238^{+0.0162}_{-0.0158}$	0.77	$0.11439^{+0.00068}_{-0.00070}$	$0.0861^{+0.0006}_{-0.0006}$	$0.600^{+0.011}_{-0.012}$	$0.025^{+0.009}_{-0.009}$	1.13
Kepler-426	3.2175	$0.8565^{+0.0280}_{-0.0275}$	$0.2157^{+0.0176}_{-0.0169}$	0.83	$0.11826^{+0.00077}_{-0.00076}$	$0.1044^{+0.0006}_{-0.0006}$	$0.725^{+0.005}_{-0.005}$	$0.039^{+0.009}_{-0.009}$	1.20
Kepler-427	10.2910	$0.8272^{+0.0045}_{-0.0044}$	$0.1890^{+0.0122}_{-0.0128}$	0.37	$0.08989^{+0.00064}_{-0.00039}$	$0.0506^{+0.0010}_{-0.0005}$	$0.158^{+0.107}_{-0.196}$	$0.172^{+0.007}_{-0.007}$	2.21
Kepler-433	5.3341	$0.8602^{+0.0058}_{-0.0061}$	$0.1725^{+0.0123}_{-0.0106}$	0.39	$0.06331^{+0.00021}_{-0.00019}$	$0.1433^{+0.0020}_{-0.0009}$	$0.052^{+0.149}_{-0.167}$	$0.059^{+0.005}_{-0.006}$	1.34
Kepler-435	8.6002	$0.8628^{+0.0066}_{-0.0063}$	$0.1881^{+0.0092}_{-0.0091}$	0.53	$0.06277^{+0.00023}_{-0.00024}$	$0.1400^{+0.0019}_{-0.0019}$	$0.422^{+0.027}_{-0.031}$	$0.059^{+0.005}_{-0.005}$	1.31
Kepler-470	24.6694	$0.8556^{+0.0088}_{-0.0091}$	$0.1632^{+0.0134}_{-0.0124}$	0.62	$0.08042^{+0.00030}_{-0.00036}$	$0.0373^{+0.0005}_{-0.0005}$	$0.429^{+0.025}_{-0.029}$	$0.220^{+0.007}_{-0.007}$	2.76
Kepler-471	5.0142	$0.8701^{+0.0071}_{-0.0075}$	$0.1664^{+0.0116}_{-0.0116}$	0.59	$0.07658^{+0.00031}_{-0.00030}$	$0.1215^{+0.0016}_{-0.0015}$	$0.415^{+0.028}_{-0.030}$	$0.082^{+0.007}_{-0.007}$	1.46
Kepler-485	3.2433	$0.8318^{+0.0027}_{-0.0025}$	$0.1890^{+0.0094}_{-0.0091}$	0.14	$0.11795^{+0.00036}_{-0.00042}$	$0.1113^{+0.0007}_{-0.0008}$	$0.196^{+0.033}_{-0.046}$	$0.030^{+0.007}_{-0.007}$	1.15
Kepler-489	17.2763	$0.7873^{+0.0058}_{-0.0059}$	$0.1971^{+0.0148}_{-0.0151}$	0.49	$0.09207^{+0.00073}_{-0.00064}$	$0.0280^{+0.0005}_{-0.0004}$	$0.250^{+0.063}_{-0.078}$	$0.110^{+0.008}_{-0.008}$	1.66
Kepler-490	3.2687	$0.8483^{+0.0038}_{-0.0037}$	$0.1958^{+0.0102}_{-0.0102}$	0.26	$0.09265^{+0.00035}_{-0.00037}$	$0.1305^{+0.0013}_{-0.0013}$	$0.265^{+0.036}_{-0.045}$	$0.020^{+0.007}_{-0.008}$	1.10
Kepler-491	4.2254	$0.8180^{+0.0055}_{-0.0056}$	$0.2287^{+0.0102}_{-0.0098}$	0.45	$0.08045^{+0.00037}_{-0.00037}$	$0.0903^{+0.0010}_{-0.0010}$	$0.449^{+0.022}_{-0.023}$	$0.033^{+0.008}_{-0.008}$	1.16
Kepler-492	11.7201	$0.8180^{+0.0318}_{-0.0302}$	$0.1931^{+0.0189}_{-0.0190}$	0.79	$0.09713^{+0.00082}_{-0.00073}$	$0.0400^{+0.0005}_{-0.0004}$	$0.699^{+0.010}_{-0.009}$	$0.217^{+0.008}_{-0.008}$	2.72
Kepler-670	2.8165	$0.8204^{+0.0042}_{-0.0043}$	$0.2081^{+0.0118}_{-0.0109}$	0.40	$0.11981^{+0.00047}_{-0.00051}$	$0.1134^{+0.0007}_{-0.0007}$	$0.413^{+0.016}_{-0.018}$	$0.015^{+0.007}_{-0.007}$	1.07
TrES-2	2.4706	$0.9213^{+0.0363}_{-0.0336}$	$0.2083^{+0.0058}_{-0.0056}$	0.85	$0.12382^{+0.00073}_{-0.00078}$	$0.1276^{+0.0005}_{-0.0005}$	$0.847^{+0.001}_{-0.001}$	$0.071^{+0.006}_{-0.006}$	1.47
HD 271181	4.2311	$0.9031^{+0.0089}_{-0.0085}$	$0.1617^{+0.0164}_{-0.0164}$	0.44	$0.08090^{+0.00039}_{-0.00037}$	$0.1305^{+0.0025}_{-0.0025}$	$0.327^{+0.051}_{-0.065}$	$0.006^{+0.002}_{-0.002}$	1.03
KELT-23	2.2553	$0.8658^{+0.0063}_{-0.0062}$	$0.1624^{+0.0090}_{-0.0084}$	0.67	$0.13299^{+0.00030}_{-0.00030}$	$0.1317^{+0.0005}_{-0.0004}$	$0.528^{+0.006}_{-0.006}$	$0.000^{+0.003}_{-0.003}$	1.00
KELT-24	5.5515	$0.8937^{+0.0022}_{-0.0022}$	$0.1434^{+0.0057}_{-0.0060}$	0.31	$0.08706^{+0.00013}_{-0.00011}$	$0.0935^{+0.0005}_{-0.0003}$	$0.003^{+0.114}_{-0.108}$	$0.013^{+0.003}_{-0.003}$	1.07
TOI-1181	2.1032	$0.8784^{+0.0054}_{-0.0053}$	$0.1599^{+0.0106}_{-0.0108}$	0.46	$0.07679^{+0.00028}_{-0.00030}$	$0.2465^{+0.0030}_{-0.0031}$	$0.321^{+0.037}_{-0.044}$	$0.006^{+0.002}_{-0.002}$	1.03
TOI-1268	8.1577	$0.8549^{+0.0081}_{-0.0084}$	$0.2091^{+0.0172}_{-0.0163}$	0.29	$0.08957^{+0.00065}_{-0.00039}$	$0.0580^{+0.0013}_{-0.0006}$	$0.046^{+0.188}_{-0.231}$	$0.014^{+0.005}_{-0.005}$	1.09
TOI-1296	3.9444	$0.8468^{+0.0087}_{-0.0092}$	$0.1734^{+0.0193}_{-0.0181}$	0.48	$0.07626^{+0.00057}_{-0.00062}$	$0.1545^{+0.0041}_{-0.0038}$	$0.278^{+0.080}_{-0.124}$	$0.009^{+0.002}_{-0.002}$	1.04
WASP-18	0.9414	$0.8780^{+0.0036}_{-0.0037}$	$0.1462^{+0.0065}_{-0.0063}$	0.46	$0.09740^{+0.00019}_{-0.00019}$	$0.2885^{+0.0014}_{-0.0013}$	$0.384^{+0.013}_{-0.014}$	$0.001^{+0.002}_{-0.002}$	1.00
WASP-62	4.4119	$0.8881^{+0.0019}_{-0.0019}$	$0.1433^{+0.0058}_{-0.0061}$	0.17	$0.11085^{+0.00019}_{-0.00019}$	$0.1031^{+0.0004}_{-0.0004}$	$0.243^{+0.017}_{-0.020}$	$0.003^{+0.002}_{-0.002}$	1.01
WASP-100	2.8494	$0.8921^{+0.0111}_{-0.0107}$	$0.1347^{+0.0091}_{-0.0092}$	0.76	$0.08269^{+0.00023}_{-0.00022}$	$0.1871^{+0.0013}_{-0.0013}$	$0.571^{+0.010}_{-0.010}$	$0.005^{+0.001}_{-0.001}$	1.02
WASP-126	3.2888	$0.8631^{+0.0044}_{-0.0044}$	$0.1970^{+0.0105}_{-0.0107}$	0.26	$0.07718^{+0.00027}_{-0.00021}$	$0.1271^{+0.0014}_{-0.0006}$	$0.047^{+0.130}_{-0.157}$	$0.005^{+0.001}_{-0.001}$	1.02

the parameters are recovered reasonably well with systematic offsets being generally within the statistical uncertainties. This demonstrates that our inferences are not only precise, but also accurate. As we can see in the figure that, except R_*/a, the uncertainties obtained from the PPDs are consistent with the Monte Carlo (MC) errorbars. The large uncertainties on R_*/a from PPDs compared to the MC estimates are due to its strong anticorrelation with P. Note that the simulated light curves contain only one transit and, hence, P is not well constrained. The light curves like the one of Kepler-5 having multiple transits constrain P well and hence the resulting uncertainty on R_*/a from PPD is substantially smaller (see Figure 3). As can be seen in the

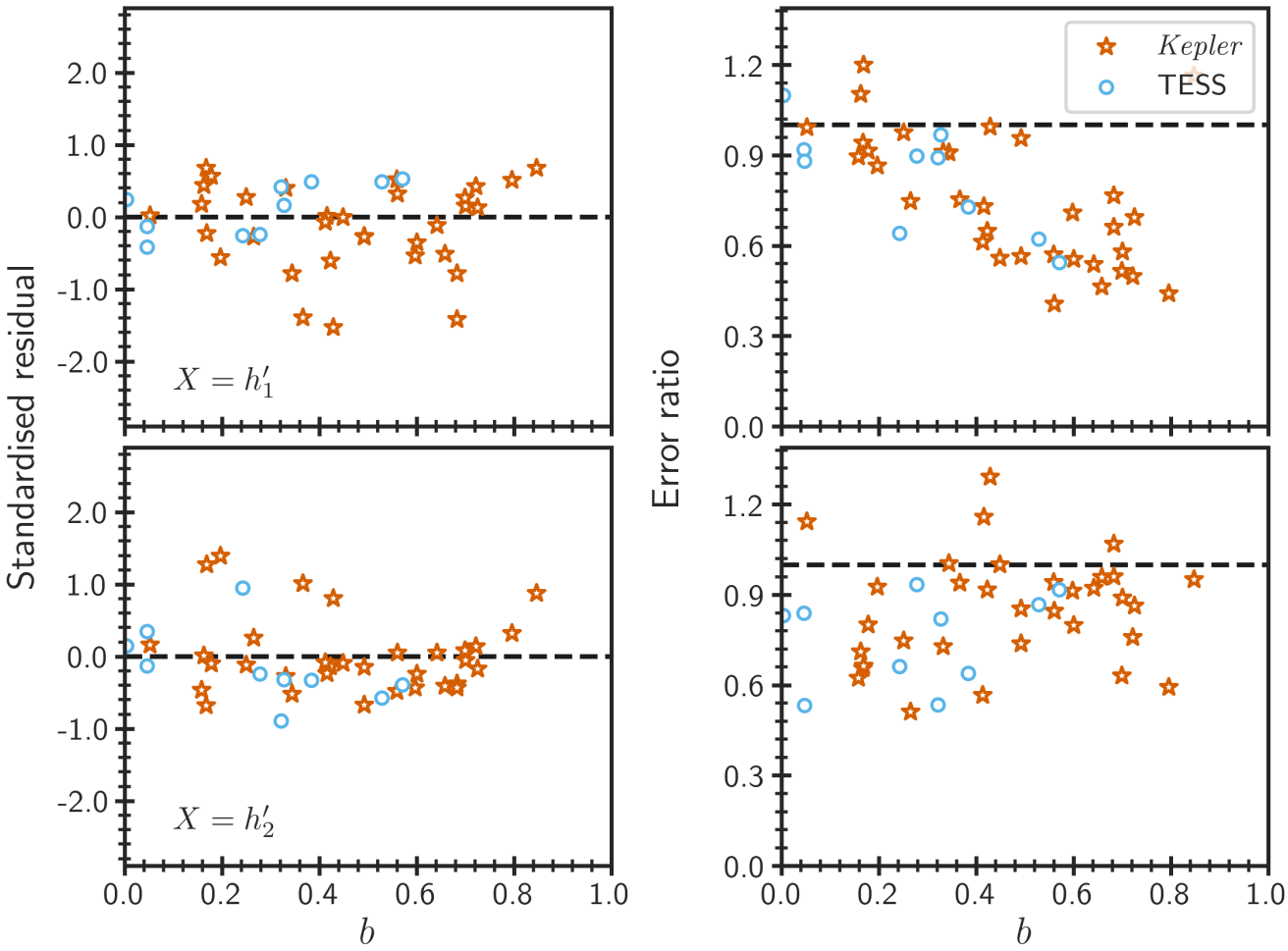

Figure 6. Comparison of our measurements of h_1' and h_2' and their associated uncertainties with those of M23 for all 43 stars in the sample. As indicated in the legend, the star and circle symbols represent the *Kepler* and TESS targets, respectively. The standardised residuals in the left column show the normalised differences between the two determinations of h_1' (top panel) and h_2' (bottom panel) as a function of the impact parameter. The dashed horizontal lines marked at zero correspond to perfect agreement. The right column presents the ratios of our and M23 uncertainties in h_1' (top panel) and h_2' (bottom panel) as a function of the impact parameter. The dashed horizontal lines marked at 1 correspond to the same uncertainties found in both studies.

figure, the correlation between h_1' and h_2' remains small for $b < 0.5$ and gradually increases beyond 0.5.

4.3 Comparison with M23

Our fitting method with $\lambda = 0$ should provide results very similar (if not identical) to those obtained by M23. We have listed the parameters for Kepler-5 found with $\lambda = 0$ in Table 1 (Work V24). The corresponding results from Table 2 of M23 are also provided in the table for the reader's convenience. At a glance, the agreement may appear reasonable, however a few discrepancies can be noticed with more careful inspection. For instance, our uncertainties on h_1' and R_p/R_* are about twice as large as those found in M23. Furthermore, the magnitude of our correlation between h_1' and h_2' is significantly larger than that of M23. We investigated these discrepancies in detail and found that they were the result of additional constraints used by M23. For every set of predicted LD coefficients $\{a_1, a_2, a_3, a_4\}$ during the fitting process, he calculated LD profile at 100 uniformly spaced μ values between 0.01 and 1, and rejected the solution if the coefficients did not correspond to a profile with $0 < I(\mu) < 1$ and $\frac{dI(\mu)}{d\mu} > 0$ for all values of μ. We performed a test with these additional constraints; the resulting parameters are also listed in the table (Work V24test). Clearly, including these constraints eliminates the discrepancies almost completely. However, since recent MHD simulations with the high surface magnetic fields predict LD profiles that are neither monotonic nor limited to $0 < I(\mu) < 1$ (Ludwig et al. 2023), we did not consider these constraints in the subsequent analysis.

Having performed various tests on simulated data and observed transit light curve of Kepler-5, we now proceed to analyse the data of other stars in our sample with $\lambda = 0.2$. Table 2 lists the resulting model parameters along with the reduced chi-square for all 43 stars. Note that the orbital period does not have any statistical errors at the fourth decimal place and the inferred parameters do not account for the tidal deformation of the planet (Burton et al. 2014; Correia 2014). To compare our results with M23, we define the standardised

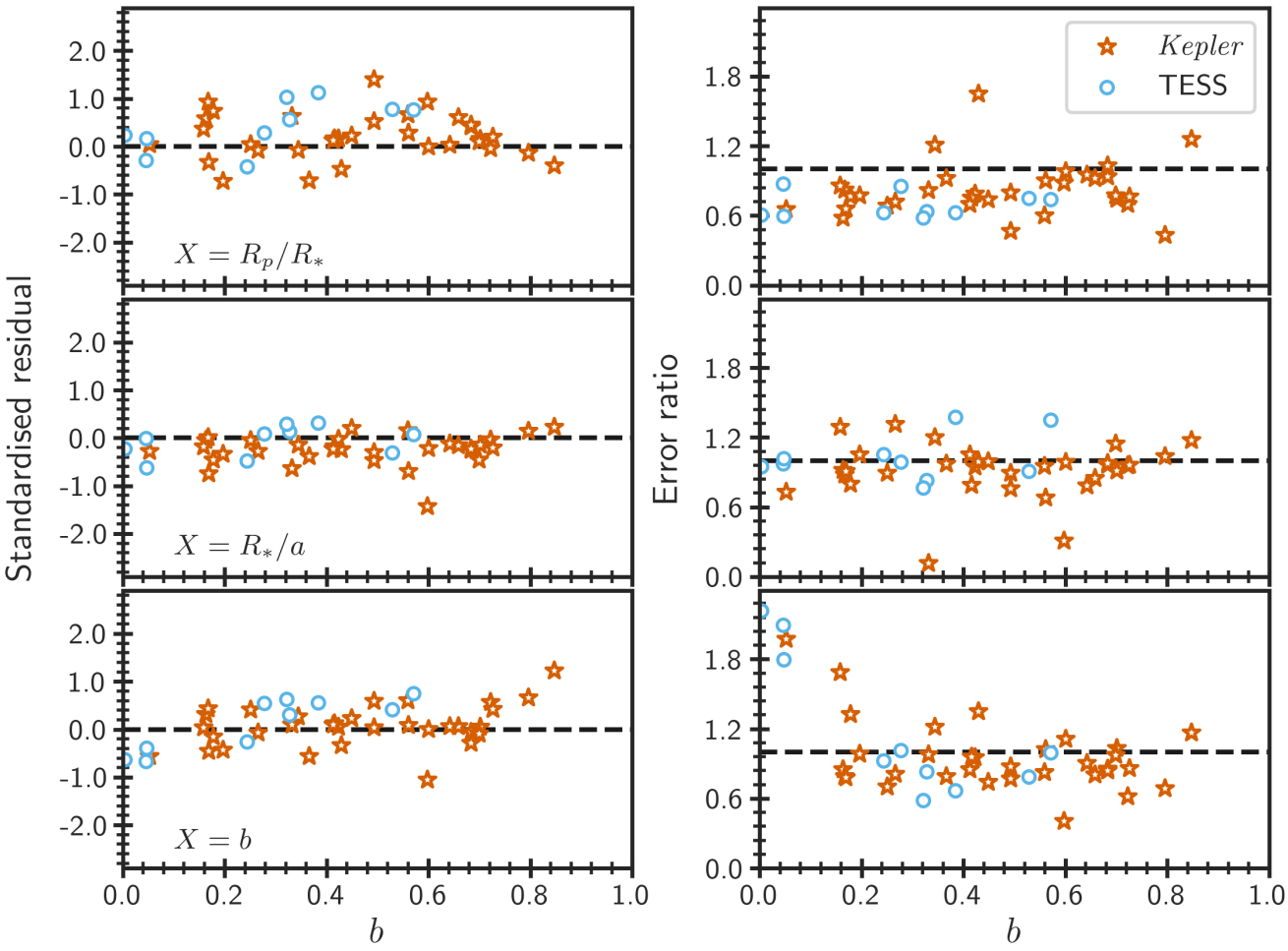

Figure 7. Same as Figure 6 except now we compare our measured R_p/R_*, R_*/a, and b and their associated uncertainties with those of M23 for all 43 stars in the sample.

residual and error ratios as,

$$\text{Standardised residual} = \frac{X_\text{V} - X_\text{M}}{\sqrt{\sigma_\text{V}^2 + \sigma_\text{M}^2}}, \tag{8}$$

and

$$\text{Error ratio} = \frac{\sigma_\text{V}}{\sigma_\text{M}}, \tag{9}$$

where X and σ refer to a specific quantity and its associated uncertainty, respectively. The subscripts V and M indicate determinations from this work and M23, respectively. As we can see in the left panels of Figure 6, the two inferences of h_1' and h_2' for all stars in our sample agree well within 2σ (for most stars, the agreement is within 1σ). Interestingly, as can be seen in the top right panel, our estimates of the uncertainty on h_1' for systems with small b are comparable to those of M23, however our h_1' becomes increasingly more precise (by up to a factor of 2) for systems with larger b. This behaviour is somewhat expected. Note that the observed transit light curves for the systems with zero or small b carry complete information about the CLV variation of the intensity. On top of this, if the photometric precision is good enough, the LD model is well constrained by the data themselves. For such targets, fitting with and without regularisation should both provide similar results. On the other hand, if b is large or the photometric precision is poor, regularisation helps significantly in constraining the LD model and leads to better precision on the inferences. From the bottom right panel, we can see that our estimates of h_2' are also more precise than those of M23 (by up to a factor of 2).

In Figure 7, we compare our determinations of R_p/R_*, R_*/a, and b with those of M23. Again, the two inferences agree well as can be seen in the left panels. Clearly, the precision of our R_p/R_* determinations is on average better than M23 by a factor of about 1.5, while the improvements in the precision of the R_*/a and b measurements are relatively modest.

4.4 Comparisons with model predictions

The 1D models of stellar atmospheres can be used to compute the CLV variations of the specific intensity as a function of the stellar parameters. We shall compare our measured h_1' and h_2' with the LD profiles calculated by Claret (2018) based on the PHOENIX-COND models (Husser et al. 2013) as well as by Kostogryz et al. (2022) based on the MPS-ATLAS models (Witzke et al. 2021). Kostogryz et al. (2022) provides two sets of LD profiles; 'Set 1' uses atmospheric models computed with the Grevesse & Sauval (1998) solar

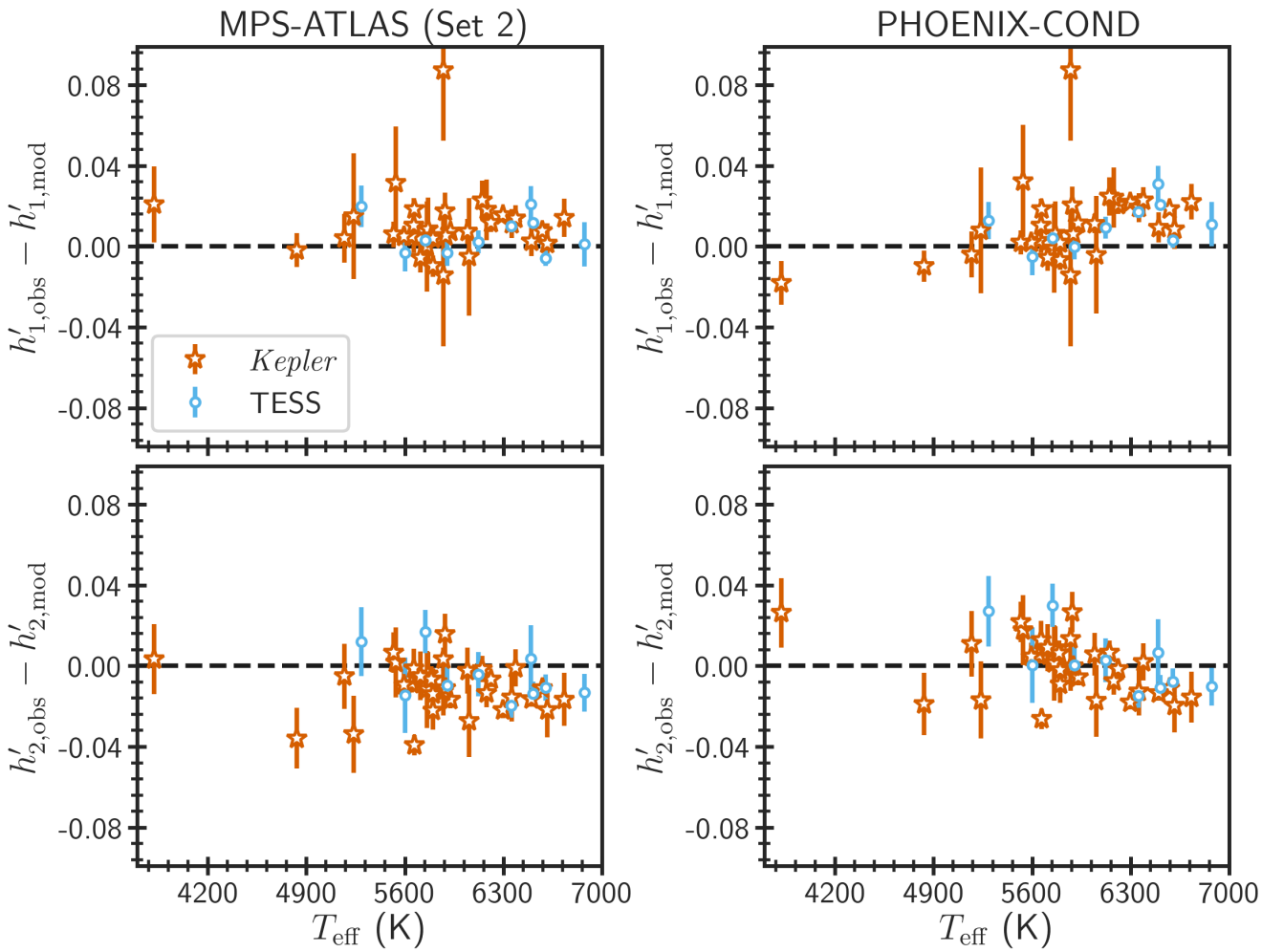

Figure 8. Comparisons of our measured h'_1 (top row) and h'_2 (bottom row) with the predictions of the MPS-ATLAS (left column) and PHOENIX-COND (right column) models for all the stars in the sample. As indicated in the legend, the star and circle symbols represent the *Kepler* and TESS targets, respectively. The dashed horizontal lines marked at zero correspond to the perfect agreement.

metallicity mixture and a fixed value of the mixing-length parameter, while 'Set 2' uses models calculated with the Asplund et al. (2009) mixture and a variable mixing-length parameter (which depends on the effective temperature). We shall compare our results with their Set 2 model predictions. The observed values of T_{eff}, $\log g$ and [Fe/H] of a star can be used to compute the corresponding predicted values of h'_1 and h'_2 through an interpolation in a grid of model LD profiles. The uncertainties in the predicted h'_1 and h'_2 due to the observational errors in T_{eff}, $\log g$ and [Fe/H] are calculated using Monte Carlo simulations. We refer the reader to M23 for further details on how the model predictions of h'_1 and h'_2 for all 43 stars were computed using the MPS-ATLAS and PHOENIX-COND atmospheric models.

Figure 8 shows comparisons of the observed h'_1 and h'_2 with various model predictions. Clearly, as can be seen in the left panels, the MPS-ATLAS models on average underestimate h'_1 and overestimate h'_2. The PHOENIX-COND models in the right panels show trends in both h'_1 and h'_2 as a function of T_{eff}, as also noted by M23. Furthermore, if we look at the differences between the observed and predicted values of h'_1 and h'_2 for individual stars, there are several discrepancies of high significance. These discrepancies can be the result of the neglect of the magnetic field in these 1D models.

Recent 3D MHD simulations of the stellar atmosphere show that the CLV variations indeed depend on the surface magnetic field, B. Using the CO^{5}BOLD code (Freytag et al. 2012), Ludwig et al. (2023, hereafter L23) constructed a set of nine MHD models assuming solar atmospheric conditions with B varying from 0 to 2400 G. The chemical composition and surface gravity of all the simulations were kept fixed at the corresponding solar values; however, the resulting T_{eff} does not necessarily correspond to the solar value and, in fact, depends on B. To isolate the effect of magnetic field, L23 developed a normalisation procedure which modifies the values of h'_1 and h'_2 of a star with non-solar atmospheric parameters to correspond to the solar conditions. For each simulation, they obtained three different sets of LD parameters: one from the light-curve fitting, the second resulting from the normalisation of the first set (corrects for differing T_{eff} only since all other parameters correspond to solar conditions), and the last from direct calculations based on the underlying Claret 4-parameter law. For further details on the MHD models, various methods to

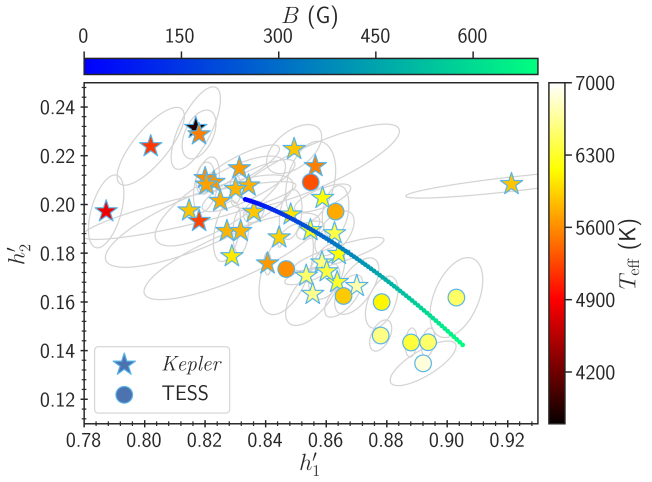

Figure 9. Comparison between the observed limb darkening and the corresponding MHD model predictions in the $h_1' - h_2'$ plane. As indicated in the legend, the star and circle symbols represent the *Kepler* and TESS targets, respectively. The ellipses around these symbols highlight the 1σ confidence regions. The associated color indicates the effective temperature of the star. The curve is a cubic function of the magnetic field which was fitted to the predictions of the MHD models normalised to the solar conditions (see the text). The color of the curve shows the strength of the magnetic field.

calculate the LD parameters, and the normalisation procedure, we refer the reader to L23.

In Figure 9, we show our measurements in the $h_1' - h_2'$ plane. There is a clear trend in the diagram; h_2' decreases as a function of h_1'. Furthermore, we can see the dependence of the LD parameters on $T_{\rm eff}$. For comparison, we also plot the L23 predictions in the form of a curve which was fitted to the results of the MHD simulations normalised to the solar conditions. Note the apparent near degeneracy between $T_{\rm eff}$ and B (both increase as we go from upper left to lower right in the figure). This is clearly an unfortunate situation for the inference of stellar magnetic field from the LD observations because this requires an accurate measurement of the effective temperature. The simulations reproduce the observational trend reasonably well; however, it is interesting to note that a slightly larger fraction of the data points lie below the model curve.

To study the effect of magnetic field on the LD and also perform cleaner comparison between the observation and simulations, we eliminate the dependence of the measured h_1' and h_2' on atmospheric parameters by normalising them to the solar conditions using the procedure of L23. The normalised observed data and simulation curves are shown in Figure 10. Note that a fraction of stars are absent in the diagram as a result of their large error regions. In this diagram, if the stars had zero magnetic field and the measurements had no errors, all the observed data points would fall to the solar position. We clearly see a trend which is qualitatively similar to what is predicted by the normalised MHD simulations. However, as noted earlier, a larger fraction of stars falls below the model curve. This is likely due to the assumed homogeneous B in the simulations, which is unrealistic. We know that the morphology of the stellar surface magnetic field is more complex with much higher field strengths in the active regions (likes stellar spots) than in the quiescent regions. As we can see in the figure, the curve corresponding to an additive mixing of two simulations with B of 50 and 1600 G fits the data trend better.

From the MHD simulations, we expect that stars with increasingly large homogeneous B follow a smooth trend extending from the upper left to the lower right in Figure 10. The results of mixing two simulations suggest that the localised high B regions such as star spots on top of the homogeneous background lead to scatters around the smooth trend. This is indeed what we see in the observed data. Among the stars on the lower right, we observe additional scatter in the light curve of Kepler-17 during transit due to random occultation of active regions by the planet (see also, Maxted 2023), thus confirming its elevated magnetic activity. However, for the rest, this signature of magnetic activity in the light curve is not observed. This does not necessarily mean that these stars have low magnetic fields. Note that if a star is near the minimum of its stellar cycle or the transit occurs at high latitudes (where we do not expect to have as many stellar spots even during the maximum), the planet may not occult any spots of significant sizes. The case of WASP-18 is particularly interesting in this regard. It is expected to have relatively high magnetic field for two reasons: (1) our limb darkening measurement (see Figure 10); and (2) its fast rotation and young age (Hellier et al. 2009) implying efficient dynamo action. However, it neither shows additional scatter in the light curve nor has been detected in X-ray observations (Pillitteri et al. 2014), thus implying a very low level of magnetic activity. A possible explanation could be that this star is going through a grand minimum of activity like the ones observed for the Sun (see e.g. Biswas et al. 2023). Recently, Lanza & Breton (2024) proposed an alternative explanation in which a massive close-by planet (such as the one WASP-18 has) can tidally induce turbulence which can inhibit the emergence of magnetic flux tubes responsible for the formation of photospheric star spots. Pillitteri et al. (2023) observed KELT-24 and, as we expect from Figure 10, they found it to be an active star showing X-ray emission.

4.5 Implications for PLATO mission

To achieve the ambitious goals of detecting and characterising Earth-like extrasolar planets orbiting around Sun-like stars in a habitable zone (potentially hosting water in a liquid state), the mission requires determination of the planet-to-star radius ratio to better than 3 per cent accuracy (Rauer et al. 2014). In this section, we wish to test whether we can determine this important quantity with required accuracy using our method. For this exercise, we used a simulated light curve for a planet with the same radius and orbital period as the Earth transiting a star with the same mass and radius as the Sun. The simulation further assumes that the orbit is circular and that the transit has a zero impact parameter. The PLATO Solar-like Light-curve Simulator (PSLS version 1.5; Samadi et al. 2019) was used to generate 1000 d of simulated data assuming the host star is observed by all 24 cameras and has an apparent magnitude of V = 10. For more details on the simulated data, we refer the reader to Section 4.4 of M23.

We fitted the simulated transit light curve using the same method as described in Section 3. We assumed a constant uncertainty of $\sigma_j = 2.5 \times 10^{-4}$ in the normalised flux to calculate the logarithm of the likelihood defined in equation (3). The resulting parameters are $P = 365.249^{+0.008}_{-0.003}$ d, $h_1' = 0.92^{+0.08}_{-0.08}$, $h_2' = 0.08^{+0.08}_{-0.08}$, $R_p/R_* = 0.00951^{+0.00024}_{-0.00029}$, $R_*/a = 0.0049^{+0.0008}_{-0.0003}$, and $b = 0.0^{+0.5}_{-0.5}$. As we can see, except for b, all quantities are reasonably well constrained. The inferred value of R_p/R_* is at about 1σ from the true value of 0.00915 and the precision of our determination is about 2.8 per cent. This clearly demonstrates that our method can provide R_p/R_* with the required accuracy.

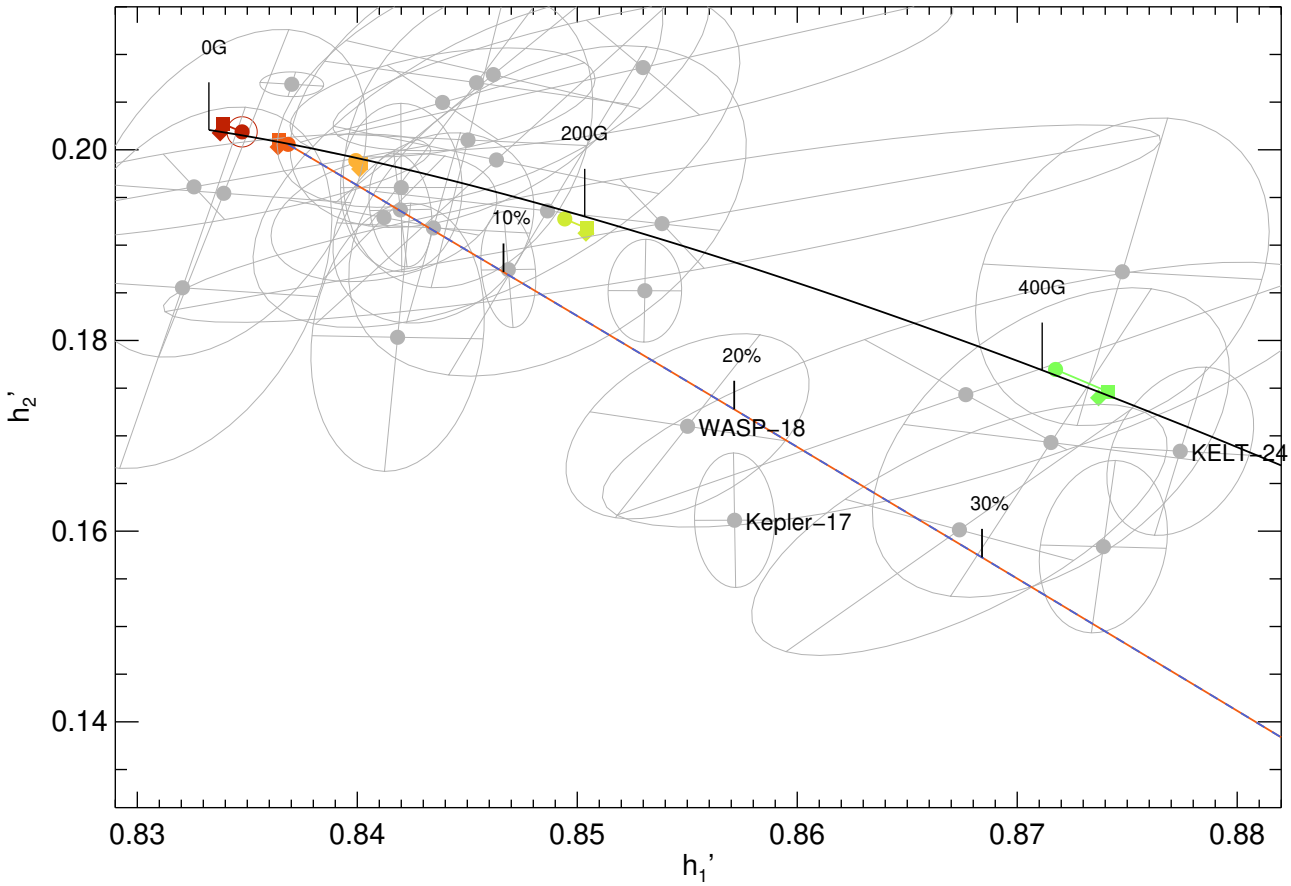

Figure 10. Comparison between the normalised observed data and corresponding MHD model predictions in the $h_1' - h_2'$ plane. The grey filled circles represent stars, and the ellipses around them highlight the 1σ confidence region. The colourful square, circle and diamond symbols depict the results of the MHD simulations as obtained from the light-curve fitting, normalisation procedure, and from the direct calculations based on the underlying Claret 4-parameter law, respectively. The data points before and after normalisation are connected by a line. The solid black curve is a cubic function of the magnetic field that was fitted to the predictions of the MHD models normalised to the solar conditions. The colorful dashed curve illustrates the outcome of an additive mixing of models with magnetic fields of 50 and 1600 G. The labeled percentages give the area fraction contributed by the simulation with 1600 G magnetic field. The best-guess solar position as obtained from the simulation with 0 G magnetic field after normalisation is marked by the solar symbol.

5 CONCLUSIONS

We developed a novel Bayesian technique to fit the transit light curves and accurately infer the planet and orbital properties and characterise the stellar limb darkening. Our BATMAN transit model used the complex nonlinear LD law but its complexity was tuned during the fitting process through a second derivative regularisation. We analysed the observed transit light curve of Kepler-5 with different values of the regularisation parameter and found that $\lambda = 0.2$ provides a good fit to the data and also results in precise LD parameters.

To test the accuracy of the inferred parameters, we applied our technique to a set of total 900 simulated transit light curves with a wide range of impact parameters computed using the BATMAN package. We found that our technique recovers parameters reasonably well, with the differences between inferred properties and the corresponding true values generally within 1σ statistical uncertainties. This exercise reassures the accuracy of our inferences. It was also shown that our uncertainty estimates from the posterior probability distribution are reliable and consistent with Monte Carlo uncertainties.

We used our validated method to analyse the transit light curves of a sample of 43 systems observed by the NASA *Kepler* and TESS missions. We found that our measurements are consistent with the latest inferences of M23 while being comparatively more precise. In particular, the errorbars on the LD parameters h_1' and h_2' are smaller than those obtained in M23 by a factor of up to 2. The precision of our inferred planet-to-star radius ratio is on average better than that of M23 by a factor of 1.5.

We compared our LD measurements with the predictions of the MPS-ATLAS and PHOENIX-COND models and found that these 1D non-magnetic models fail to reproduce the observations. As seen in the $h_1' - h_2'$ diagram, the predictions of the 3D MHD simulations follow the same trend as the observations; however, there is still noticeable discrepancy, as relatively more data points lie below the model curve. To remove the impact of the atmospheric parameters on the limb darkening and perform a more consistent comparison between the model and observation, we normalised the observed data to solar conditions following the procedure of L23. We found that the above discrepancy persists. We attributed the origin of this problem to our unrealistic choice of homogeneous magnetic field in the simulations. We showed that a physically more realistic model corresponding to an additive mixing of two simulations with magnetic fields of 50 and 1600 G fits the data better. Our precise measurements of the LD together with MHD simulations confirm that Kepler-17, WASP-18 and KELT-24 have relatively high magnetic fields (> 200 G). This study demonstrates that we can potentially estimate the stel-

lar surface magnetic field by calibrating the observed LD against the predictions of realistic MHD simulations of varying magnetic field.

Finally, we performed a test using the simulated light curve of a planet with the same radius and orbital period as the Earth transiting a star with the same mass and radius as the Sun to show that our technique can be used to infer the planet-to-star radius ratio with the accuracy required for the ESA PLATO mission.

ACKNOWLEDGEMENTS

This research was supported by the Munich Institute for Astro-, Particle and BioPhysics (MIAPbP) which is funded by the Deutsche Forschungsgemeinschaft (DFG, German Research Foundation) under Germany´s Excellence Strategy – EXC-2094 – 390783311. The support and the resources provided by PARAM Shivay Facility under the National Supercomputing Mission, Government of India at the Indian Institute of Technology, Varanasi are gratefully acknowledged.

DATA AVAILABILITY

The data underlying this article will be shared on reasonable request to the corresponding author.

REFERENCES

Asplund M., Grevesse N., Sauval A. J., Scott P., 2009, ARA&A, 47, 481
Biswas A., Karak B. B., Usoskin I., Weisshaar E., 2023, Space Sci. Rev., 219, 19
Borucki W. J., et al., 2010, Science, 327, 977
Brooks S., Gelman A., Jones G., Meng X.-L., 2011, Handbook of Markov Chain Monte Carlo. CRC press
Burton J. R., Watson C. A., Fitzsimmons A., Pollacco D., Moulds V., Littlefair S. P., Wheatley P. J., 2014, ApJ, 789, 113
Claret A., 2000, A&A, 363, 1081
Claret A., 2018, A&A, 618, A20
Claret A., Hauschildt P. H., 2003, A&A, 412, 241
Correia A. C. M., 2014, A&A, 570, L5
Csizmadia S., Pasternacki T., Dreyer C., Cabrera J., Erikson A., Rauer H., 2013, A&A, 549, A9
Diaz-Cordoves J., Gimenez A., 1992, A&A, 259, 227
Espinoza N., Jordán A., 2016, MNRAS, 457, 3573
Foreman-Mackey D., 2016, The Journal of Open Source Software, 1, 24
Foreman-Mackey D., Hogg D. W., Lang D., Goodman J., 2013, PASP, 125, 306
Freytag B., Steffen M., Ludwig H. G., Wedemeyer-Böhm S., Schaffenberger W., Steiner O., 2012, Journal of Computational Physics, 231, 919
Gardner J. P., et al., 2006, Space Sci. Rev., 123, 485
Gelman A., Carlin J., Stern H., Dunson D., Vehtari A., Rubin D., 2013, Bayesian Data Analysis, Third Edition. Chapman & Hall/CRC Texts in Statistical Science, Taylor & Francis, https://books.google.dk/books?id=ZXL6AQAAQBAJ
Gilmozzi R., Spyromilio J., 2007, The Messenger, 127, 11
Goodman J., Weare J., 2010, Communications in Applied Mathematics and Computational Science, 5, 65
Grevesse N., Sauval A. J., 1998, Space Sci. Rev., 85, 161
Hellier C., et al., 2009, Nature, 460, 1098
Hestroffer D., 1997, A&A, 327, 199
Hogg D. W., Foreman-Mackey D., 2018, ApJS, 236, 11
Howarth I. D., 2011, MNRAS, 418, 1165
Husser T. O., Wende-von Berg S., Dreizler S., Homeier D., Reiners A., Barman T., Hauschildt P. H., 2013, A&A, 553, A6
Jaynes E. T., 2003, Probability Theory: The Logic of Science. Cambridge University Press: Cambridge
Klinglesmith D. A., Sobieski S., 1970, AJ, 75, 175
Kopal Z., 1950, Harvard College Observatory Circular, 454, 1
Kostogryz N. M., Witzke V., Shapiro A. I., Solanki S. K., Maxted P. F. L., Kurucz R. L., Gizon L., 2022, A&A, 666, A60
Kostogryz N. M., et al., 2024, arXiv e-prints, p. arXiv:2403.00118
Kreidberg L., 2015, PASP, 127, 1161
Lanza A. F., Breton S. N., 2024, arXiv e-prints, p. arXiv:2404.08439
Ludwig H. G., Steffen M., Freytag B., 2023, A&A, 679, A65
Maxted P. F. L., 2018, A&A, 616, A39
Maxted P. F. L., 2023, MNRAS, 519, 3723
Milne E. A., 1921, MNRAS, 81, 361
Morello G., Tsiaras A., Howarth I. D., Homeier D., 2017, AJ, 154, 111
Müller H. M., Huber K. F., Czesla S., Wolter U., Schmitt J. H. M. M., 2013, A&A, 560, A112
Neilson H. R., McNeil J. T., Ignace R., Lester J. B., 2017, ApJ, 845, 65
Norris C. M., Beeck B., Unruh Y. C., Solanki S. K., Krivova N. A., Yeo K. L., 2017, A&A, 605, A45
Patel J. A., Espinoza N., 2022, AJ, 163, 228
Pillitteri I., Wolk S. J., Sciortino S., Antoci V., 2014, A&A, 567, A128
Pillitteri I., Colombo S., Micela G., Wolk S. J., 2023, A&A, 673, A61
Rauer H., et al., 2014, Experimental Astronomy, 38, 249
Ricker G. R., et al., 2015, Journal of Astronomical Telescopes, Instruments, and Systems, 1, 014003
Samadi R., et al., 2019, A&A, 624, A117
Sharma S., 2017, ARA&A, 55, 213
Sing D. K., Vidal-Madjar A., Désert J. M., Lecavelier des Etangs A., Ballester G., 2008, ApJ, 686, 658
Tinetti G., et al., 2018, Experimental Astronomy, 46, 135
Witzke V., et al., 2021, A&A, 653, A65

APPENDIX A: SENSITIVITY TO REGULARISATION PARAMETER

In this section, we show the results obtained with values of regularisation parameter in the neighbourhood of the reference value of 0.2. In Figure A1, we compare our estimates of h'_1, h'_2 and their associated uncertainties found with $\lambda = 0.5$ with the corresponding determinations of M23. In the right panels, it is clear that the measurement precision has improved; however, we notice a small bias in the left panels. In Figure A2, we show the same but now the analysis was performed with $\lambda = 0.1$. With this value of λ, we almost completely get rid of the bias, but loose the precision significantly. This behaviour is clearly expected.

This paper has been typeset from a TEX/LATEX file prepared by the author.

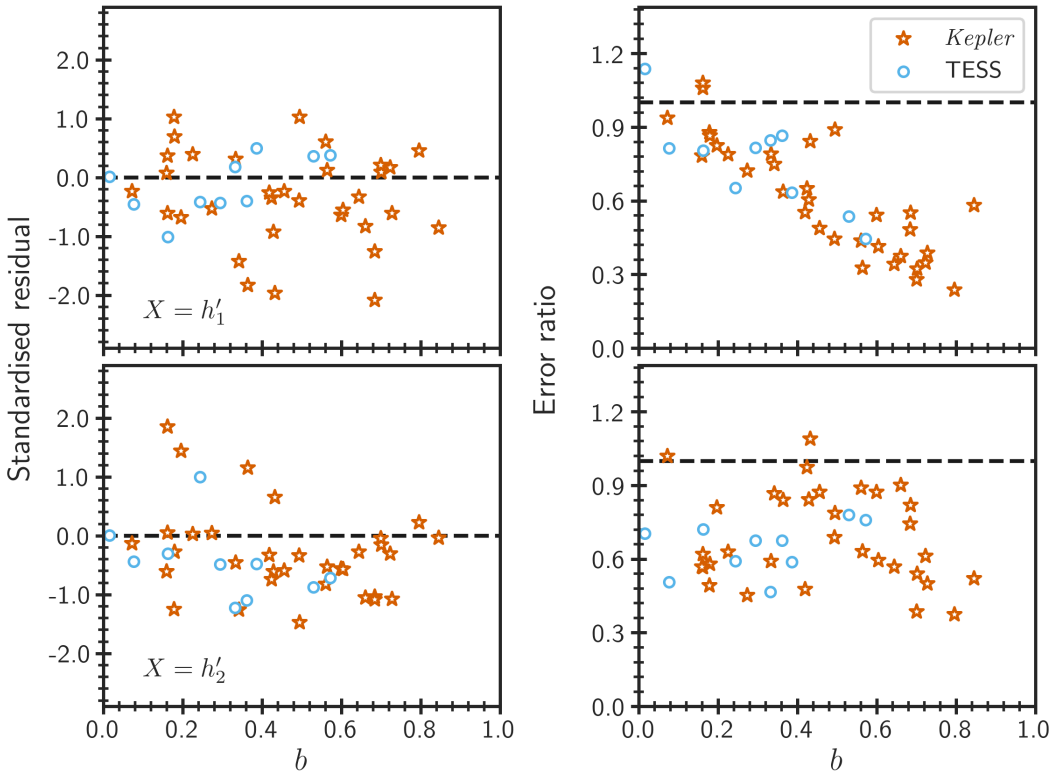

Figure A1. Same as Figure 6 except the analysis was performed with $\lambda = 0.5$ (instead of 0.2).

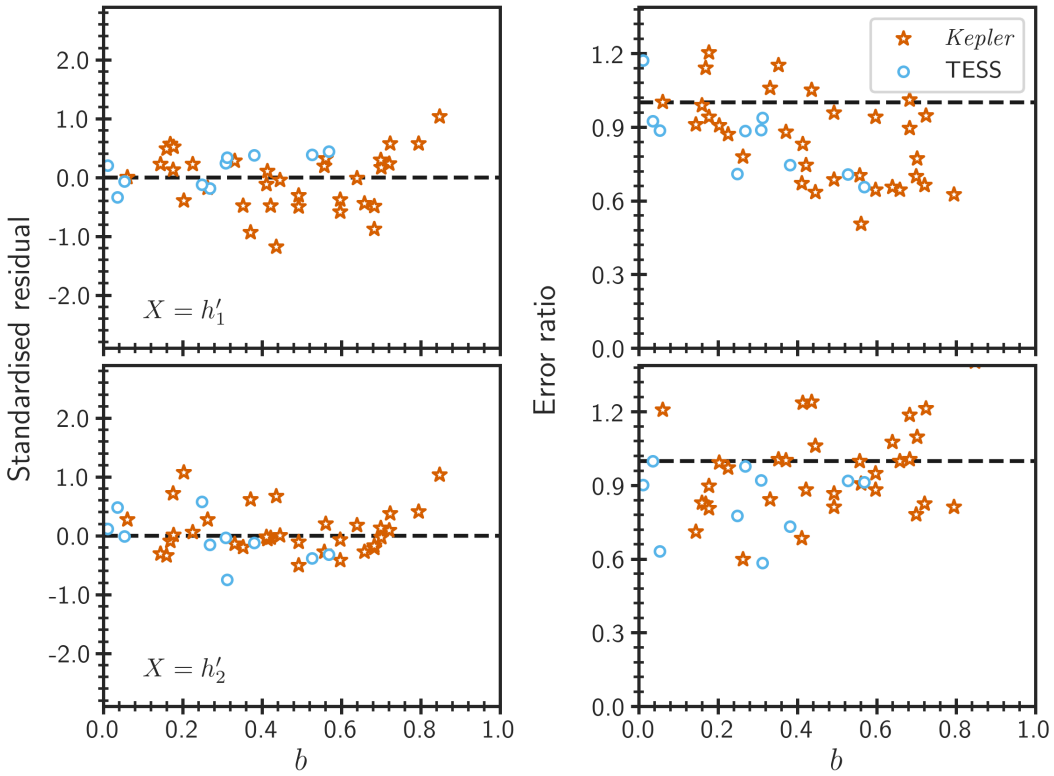

Figure A2. Same as Figure 6 except the analysis was performed with $\lambda = 0.1$ (instead of 0.2).